International Journal of Nanomedicine

Dovepress
open access to scientific and medical research

Open Access Full Text Article

ORIGINAL RESEARCH

Tumor-Targeted Polydopamine-Based Nanoparticles for Multimodal Mapping Following Photothermal Therapy of Metastatic Lymph Nodes

Yanrui Liang[1,*], Weihong Guo[1,*], Chuangji Li[1,*], Guodong Shen[1,*], Haoxian Tan[2], Peiwen Sun[2], Zhian Chen[1], Huilin Huang[1], Zhenhao Li[1], Zhenyuan Li[1], Yingxin Ren[1], Guoxin Li[1], Yanfeng Hu[1]

[1]Department of General Surgery & Guangdong Provincial Key Laboratory of Precision Medicine for Gastrointestinal Tumor, Nanfang Hospital, Southern Medical University, Guangzhou, People's Republic of China; [2]The First School of Clinical Medicine, Southern Medical University, Guangzhou, People's Republic of China

*These authors contributed equally to this work

Correspondence: Guoxin Li; Yanfeng Hu, Department of General Surgery & Guangdong Provincial Key Laboratory of Precision Medicine for Gastrointestinal Tumor, Nanfang Hospital, Southern Medical University, No. 1838 North Guangzhou Ave, Baiyun District, Guangzhou, 510515, People's Republic of China, Tel +86-20-6164-1681; +86-20-6164-1682, Fax +86-20-6164-1681, Email yfenghu@qq.com; gzliguoxin@163.com

Purpose: Lymphadenectomy with lymph node (LN) mapping is essential for surgical removal of solid tumors. Existing agents do not provide accurate multimodal mapping and antitumor therapy for metastatic LNs; therefore, we fabricated a polydopamine (PDA) nanoparticle (NP)-based tumor-targeted LN mapping agent capable of multimodal mapping and guided photothermal therapy (PTT) for metastatic LNs.

Materials and Methods: PDA NPs modified with polyethylene glycol (PEG) were obtained by polymerization under alkaline conditions. The PEG-PDA NPs were loaded with the circular tripeptide Arg-Gly-Asp (cRGD) to achieve tumor-targeting capacity and with the fluorescent dye IR820 and magnetic resonance imaging (MRI) contrast $Gd(NH_2)_2$ for in situ detection. The resulting cRGD-PEG-PDA@IR820/$Gd(NH_2)_2$ (cRGD-PPIG) NPs were tested for their biosafety and metastatic LN mapping ability. They were drained specifically into LNs and selectively taken up by gastric MKN45 cells via $\alpha_v\beta3$ integrin-mediated endocytosis.

Results: This phenomenon enabled MR/optical/near-infrared fluorescence multimodal metastatic LN mapping, guiding the creation of accurate and highly efficient PTT for gastric cancer metastatic LNs in mice.

Conclusion: In summary, we fabricated tumor-targeted cRGD-PPIG NPs with MR/optical/near-infrared fluorescence multimodal metastatic LN mapping capacity for surgery and efficient PTT guidance post-surgery.

Keywords: multimodal imaging, lymph node mapping, metastatic lymph node, photothermal therapy

Introduction

Cancer is one of the main global public health issues, with 24.5 billion cases and 9.6 million deaths reported worldwide in 2017.[1] Radical lymphadenectomy is essential for solid tumor removal, but to succeed, it requires perioperative visualization and identification of lymph nodes (LNs).[2–5] LN mapping is important for gastrointestinal tumors, owing to the complex lymphatic drainage system of the digestive tract.[6] Patient prognosis is improved if more LNs, especially metastatic LNs, are resected.[7–9] Thus, targeted metastatic LN mapping and treatment should be more accurate and efficient.

Several methods have been applied to map LNs. Magnetic resonance imaging (MRI) has been widely used to diagnose LNs before surgery due to the sensitivity of the technique to soft tissue lesions.[10,11] Primary and metastatic lesions show an increase in signal intensity on diffusion-weighted imaging compared to normal structures.[12] Dyes such as nanocarbon particles and indocyanine green are used during surgery to visualize LNs. Nanocarbon particles enable convenient optical imaging of LNs, whereas indocyanine green can stain both LNs and the lymphatic route.[13–16] Nevertheless, existing LN mapping agents have intrinsic defects, which limit their clinical application. First, the lack

Received: 5 May 2022
Accepted: 7 September 2022
Published: 29 September 2022

of a multimodal LN mapping ability lowers the accuracy.[17] Second, the lack of tumor-targeting ability prevents their use in precision medicine.[18] Finally, the lack of therapeutic effects hinders their clinical application.[19] Thus, a tumor-targeted multimodal LN mapping agent is required to successfully integrate the diagnosis and treatment of solid tumors.

The clinical requirements of LN mapping agents may be met through nanotechnology, as suggested by the numerous nanoprobes designed for multimodal LN mapping and treatment. Yang et al[20] designed perylene diimide probes of different sizes for LN positron emission tomography and photoacoustic imaging. Shi et al[19] designed tumor-targeted CuS nanoparticles (NPs) for LN fluorescence/computed tomography imaging and guided photothermal therapy (PTT). Ideally, to facilitate greater convenience in clinical applications, multimodal imaging should include optical imaging, for which NPs with a natural black color may be good candidates. Polydopamine (PDA) NPs, with their non-toxic semiconducting dopamine molecules, have emerged as a promising and powerful nanoplatform with broad biological application prospects.[21] Owing to their relevant physicochemical properties, such as coloration,[22] easy functionalization,[23] elevated drug loading efficacy,[24] high metal-chelation ability,[25] and ultrafast thermal relaxation,[26] PDA NPs have been widely applied in tumor imaging. Furthermore, PDA NPs of different sizes can be easily obtained by adjusting the pH during dopamine self-assembly.[27,28]

In this study, we aimed to produce multimodal NPs that can meet the requirements for accuracy, efficacy, and ease of use necessary in clinical tumor imaging. We synthesized PDA-based NPs containing polyethylene glycol (PEG), a tumor-targeted ligand consisting of a circular-arginine-glycine-aspartic acid sequence (cRGD), a near-infrared (NIR) organic dye (IR820) and clinical MRI contrast $Gd(NH_2)_2$. The size of the resulting cRGD- PEG-PDA@IR820/$Gd(NH_2)_2$ (cRGD-PPIG) NPs (50–250 nm) aided specific draining into lymph vessels rather than the bloodstream, as reported previously.[28,29] Owing to their coloration and good photothermal conversion efficiency, PDA NPs were employed as probes for the optical diagnosis of metastatic LNs and PTT. In addition, PDA NPs loaded with $Gd(NH_2)_2$ and IR820 were used for metastatic LN MR and fluorescence imaging. Essentially, this study demonstrates the application of PDA NPs for MR/optical/NIR fluorescence multimodal tumor-targeted LN mapping and PTT.

Materials and Methods

Chemistry

Reagents and Instrumentation

Dopamine hydrochloride (98%; Aladdin, Shanghai, China), gadodiamide ($Gd(NH_2)_2$, OMNISCAN, GE Healthcare, Cork, Ireland), and IR820 (C46H50ClN2NaO6S2, 80%; Macklin, Shanghai, China) were purchased from Casmart and Rjmart platforms. The cRGD ligand and PEG (NH_2-mPEG-COOH, MW 5000, 98%) were purchased from Guangzhou Tanshui Co., Ltd. (Guangzhou, China). Fetal bovine serum (FBS), Dulbecco's modified Eagle medium (DMEM), penicillin-streptomycin solution, and trypsin-EDTA were obtained from Thermo Fisher Scientific (Waltham, MA, USA). Phosphate-buffered saline (PBS), 5-ethynyl-2' DNA nucleoside uracil (EdU), 4′,6-diamidino-2-phenylindole (DAPI), reactive oxygen species (ROS) test kit, and Cell Counting Kit-8 (CCK-8) were purchased from Beyotime (Shanghai, China). Transmission electron microscopy (TEM) images were acquired using a JEM-2100F microscope (JEOL, Japan). Dynamic light scattering (DLS) and zeta potential were measured on a Zetasizer Nano ZS (Malvern, UK). A UV-2600 spectrophotometer (Shimadzu, Japan) was used to acquire UV-vis absorption spectra. Semiconductor lasers at 808 nm were purchased from Shanghai Xilong Optoelectronics Technology Co., Ltd. (Shanghai, China). Optical and NIR fluorescence imaging of nude mouse LNs were performed using white (380–665 nm) and NIR (810–1200 nm) light via a dual-channel image-guided device. An infrared thermal camera (E50; FLIR, USA) was used to acquire thermal images.

^{1}H NMR spectra were recorded using a 500 MHz Bruker Avance III spectrometer (Bruker, Billerica, MA, USA).

Synthesis of PDA NPs

Briefly, 432 mg dopamine hydrochloride (2.28 mmol) was dissolved in 216 mL deionized water. PDA NPs were obtained upon addition of 2280 μL NaOH (1 N) and vigorous stirring at 50 °C for 10 h. The solution was then centrifuged at 14000 rpm and 26 °C for 10 min, followed by three washes with deionized water.

Surface Modification of PDA NPs with NH_2-PEG_{5000}-COOH

We adjusted the pH of a 10 mL PDA aqueous solution (2 mg/mL in water) to 9, and added 30 mg NH_2-PEG_{5000}-COOH. PEG-modified PDA was retrieved via centrifugation at 14,000 rpm after vigorous stirring, and was then washed several times with deionized water. After freeze-drying, the aqueous solvent was removed and powdered PEG-PDA NPs were obtained.

Loading of the cRGD Ligand

We mixed 1-(3-dimethylaminopropyl)-3-ethylcarbodiimide hydrochloride (EDC) and N-hydroxysulfosuccinimide sodium salt (sulfo-NHS) with PEG-PDA NPs. The mixture was stirred at 26 °C for 4 h and then washed several times. NH_2-cRGD (4 mg) was added to the suspension at room temperature. Finally, the unreacted cRGD was removed, and the solution was washed several times with PBS.

Loading of PEG-PDA NPs with IR820 and $Gd(NH_2)_2$

We mixed the IR820 solution with a PEG-PDA NP aqueous solution or cRGD-PEG-PDA NP aqueous solution and allowed it to react for 6 h in the dark. The IR820:PEG-PDA NP weight ratio was 0.04:1, the same as the IR820:cRGD-PEG-PDA NP weight ratio. The formed NPs were centrifuged at 14,000 rpm and 26 °C for 10 min and then washed several times with deionized water. The loading efficiency (weight of loaded IR820/weight of added IR820 × 100%) and loading content (weight of loaded IR820/[weight of loaded IR820 + weight of NPs] × 100%) of IR820 on NPs were calculated by measuring unloaded and free IR820 in a UV-vis-NIR spectrophotometer. Thereafter, $Gd(NH_2)_2$ was loaded onto PEG-PDA@IR820 NPs. Briefly, freshly prepared $Gd(NH_2)_2$ solution was mixed with PEG-PDA@IR820 NPs at a $Gd(NH_2)_2$/PEG-PDA@IR820 NP weight ratio of 0.04:1. After 6 h of reaction, the mixture was centrifuged at 14,000 rpm and 26 °C for 10 min to remove free $Gd(NH_2)_2$. We analyzed the amount of $Gd(NH_2)_2$ loaded onto the NPs using inductively coupled plasma mass spectrometry. The photothermal properties of NPs of different sizes were measured in 200 μL PBS inside Eppendorf tubes after irradiation with a NIR laser at 808 nm (FC-808-10W-MM; Xilong Company, China) and a power density of 0.25–1 W/cm^2 for 5 min. Real-time thermal images were recorded with an IR thermal camera (225–1; Fotric, China) and the corresponding temperature was determined. The generated NPs were denoted as PEG-PDA@IR820/ $Gd(NH_2)_2$ NPs (PPIG NPs) and cRGD-PEG-PDA@IR820/ $Gd(NH_2)_2$ NPs (cRGD-PPIG NPs).

In vitro Experiments

Cell Culture

Mouse axillary lymph node/vascular epithelial cells (SVEC4-10), human normal gastric epithelial cells (GES-1), and gastric cancer cells (MKN45) were purchased from the American Type Culture Collection (USA). All three cell lines were cultured and maintained in DMEM supplemented with 10% FBS and antibiotics (100 U/mL) at 37 °C in 5% CO_2. Cells were seeded in 6- or 96-well plates.

Confocal Laser Scanning Microscopy

MKN45 cells were seeded in confocal laser scanning microscopy (CLSM) dishes and cultured for 24 h in DMEM supplemented with 10% FBS. To determine whether integrin alpha V beta 3 ($\alpha_v\beta3$) was expressed on the cell surface, MKN45 cells were washed, fixed with 4% paraformaldehyde, and incubated with 5% bovine serum albumin (Gibco, USA). The cells were then incubated with anti-integrin $\alpha_v\beta3$ antibody (LM609; Abcam, China) overnight at 4 °C. After incubation with secondary antibodies, the cells were stained with DAPI (Beyotime) and observed using CLSM (Olympus, Japan). To assess cRGD-PPIG NP absorption, MKN45 cells were incubated with PPIG NPs or cRGD-PPIG NPs for 24 h, washed, fixed with 4% paraformaldehyde, stained with DAPI, and observed using CLSM.

Flow Cytometry

MKN45 cells were seeded in 6-well plates (1 X 10^6 cells) and cultured for 24 h. The cells were then incubated with PPIG NPs (100 ug/mL) or cRGD-PPIG NPs (100 ug/mL) for 24 h, harvested, suspended, and analyzed using flow cytometry.

CCK-8 Assay

SVEC4-10 cells were seeded in 96 well plates at 5×10^5 cells/well and cultured for 24 h, and then incubated with cRGD-PPIG NPs at varying concentrations (range from 0–100 ug/mL) for an other 24 h. Thereafter, the biosafety of cRGD-PPIG NPs was

assayed using a CCK-8 detection kit following the manufacturer's instructions. Biosafety was determined based on the cell viability ratio of exposed cells relative to the blank control.

To detect the antitumor effect of cRGD-PPIG NPs, MNK45 cells were seeded in 96-well plates at 5×10^5 cells/well and cultured for 24 h. Subsequently, the cells were divided into equal groups and exposed to one of the six following treatments: the control treatment (DMEM with 10% FBS), PPIG treatment (free PPIG NPs at varying concentrations (ranging from 0–100 μg/mL)), cRGD-PPIG treatment (free cRGD-PPIG NPs at varying concentrations (ranging from 0–100 μg/mL)), NIR treatment (DMEM with 10% FBS, and irradiation at 1 W/cm^2 for 5 min), PPIG at varying concentrations (ranging from 0–100 μg/mL) + NIR treatment (1 W/cm^2, 5 min), and cRGD-PPIG at varying concentrations (ranging from 0–100 μg/mL) + NIR treatment (1 W/cm^2 for 5 min). After treatment, we used the CCK-8 assay to determine cell viability.

EdU Assay

The antitumor effect of cRGD-PPIG NPs with and without NIR was assessed using an EdU assay (KeyGen, China). Briefly, 6×10^5 MKN45 cells were seeded in 12-well plates and cultured overnight. Thereafter, the cells were incubated with the same concentrations of PPIG NPs (100 μg/mL) and cRGD-PPIG NPs (100 μg/mL), and subjected or not subjected to NIR irradiation (1 W/cm^2, 5 min). Based on the manufacturer's instructions, treated cells were labeled, fixed, stained, and finally monitored using CLSM.

ROS Assay

MKN45 cells were seeded in 6-well plates (1 X 10^6 cells) and cultured for 24 h. The cells were treated with PPIG NPs (100 μg/mL) or cRGD-PPIG NPs (100 μg/mL) for 24 h, with or without NIR irradiation (1 W/cm^2, 5 min). Finally, the cells were incubated with ROS Assay Kit reagents (Beyotime) and analyzed using flow cytometry.

In vivo Experiments

Animals

Nude mice and Sprague-Dawley rats were obtained from the Biomedical Research Institute of Southern Medical University. Animal experiments and euthanasia were performed following approval by the Institutional Animal Care and Use Committee of Southern Medical University (Certification No. K2020015). All procedures conducted in animals complied with the Animal Welfare Act, the Guide for the Care and Use of Laboratory Animals, and the Office of Laboratory Animal Welfare.

In vivo PTT Effect

To clarify the therapeutic effect of cRGD-PPIG NPs, we first established tumor-bearing mice by injecting MKN45 cells (50 μL, 2×10^7 cells/mL) into the left hind foot sole of nude mice (n =30). After 28 days, the left popliteal LNs were swollen, indicating the presence of metastatic LNs. PBS (in the control group), PPIG NPs, or cRGD-PPIG NPs were injected peritumorally once, with or without NIR irradiation, into the metastatic LNs (1 W /cm^2, 5 min, once). An infrared 225–1 thermal camera was used to record real-time temperature changes in vivo. Ten days after NIR irradiation, metastatic LNs were excised for immunofluorescence staining using terminal deoxynucleotidyl transferase dUTP nick end labeling (TUNEL; Abcam, USA).

In vivo Biodistribution and Biosafety

For in vivo biodistribution analysis, we injected the left rear footpad of nude mice (n = 3/group) with 50 μL PBS containing 50 μg of cRGD-PPIG NPs or PPIG NPs. One hour after injection, the mice were sacrificed using an overdose of pentobarbital. Thereafter, the major organs were excised and imaged. To quantitatively evaluate and compare the toxicity of cRGD-PPIG NPs, Sprague-Dawley rats (n = 3/group) were injected with 100 μL PBS containing 350 μg cRGD-PPIG NPs or PPIG NPs. Thereafter, biochemical blood indices, including alanine transaminase, aspartate transaminase, blood urea nitrogen, and creatinine, were measured using enzyme-linked immunosorbent assay kits.

Statistical Analysis

Data are expressed as the mean ± standard deviation. All experiments were repeated at least thrice. We used the unpaired Student's *t*-test or analysis of variance followed by Scheffe's post-hoc test to evaluate the data. Differences were considered statistically significant at $p < 0.05$.

Results and Discussion

Design of cRGD-PPIG MR/NPs for Optical/NIR Fluorescence Multimodal Tumor-Targeted LN Mapping and PTT

Scheme 1 shows the design and polymerization of PDA NPs, their functionalization with PEG, and cRGD ligand, MRI contrast ($Gd(NH_2)_2$), and NIR dye (IR820) loading. PDA NPs were selected as optical imaging agents because of their black coloration, easy functionalization, and low systemic toxicity.[21] Hydrophilic PEG_{5000} was introduced into the outer shell of PDA NPs to improve biocompatibility,[30] the cRGD ligand conferred tumor-targeting capability, and $Gd(NH_2)_2$ and IR820 facilitated sensitive LN MR/fluorescence imaging in vivo.[31] The generated cRGD-PPIG NPs were injected locally and specifically mapped to the left metastatic popliteal LN to aid MR, optical and NIR fluorescence imaging, and PTT.

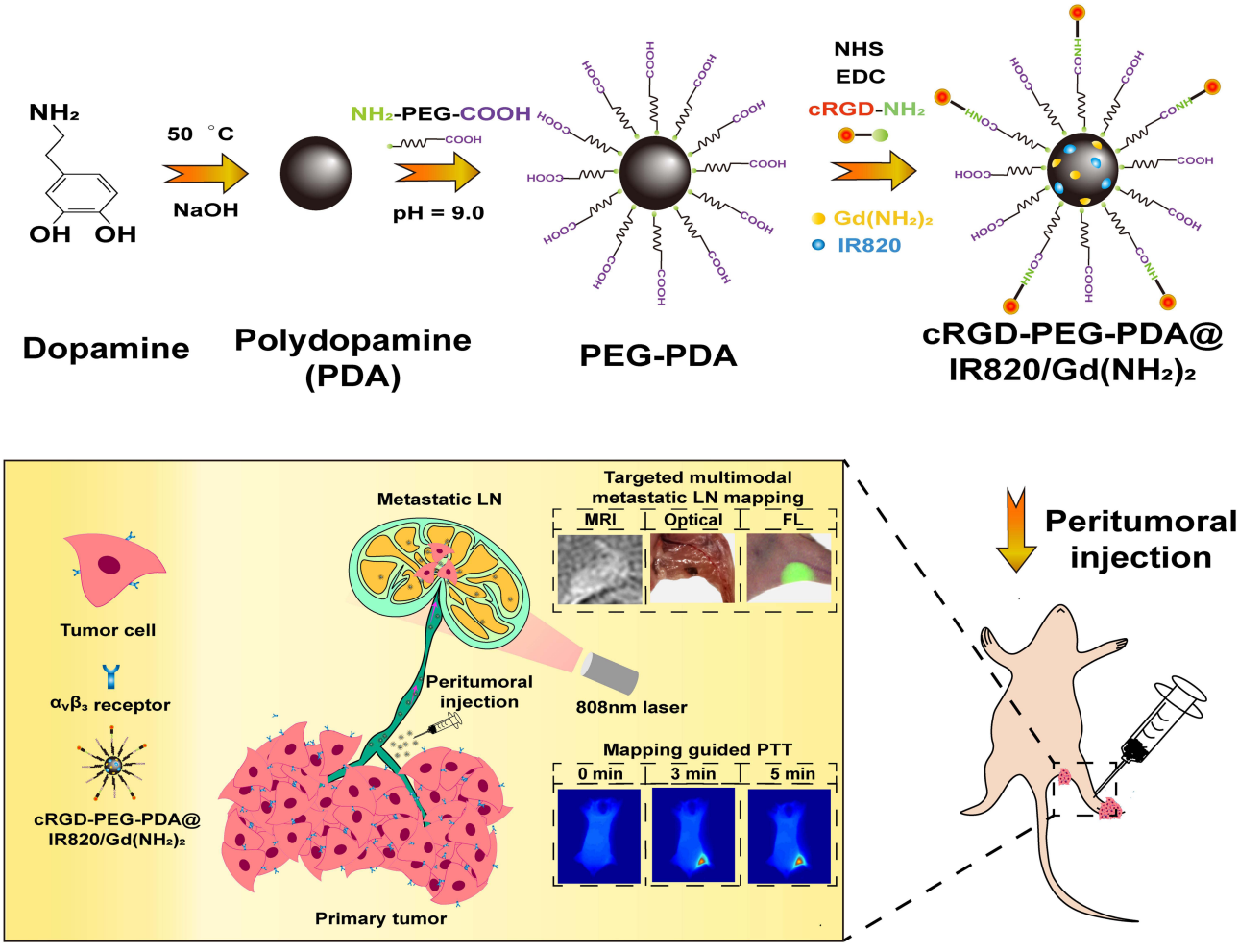

Scheme 1 Design of cRGD-PPIG NPs for LN MR/optical/NIR fluorescence multimodal imaging and PTT. Schematic illustration of the design and synthesis of cRGD-PEG-PDA@IR820/ $Gd(NH_2)_2$ NPs. The generated cRGD-PPIG NPs were injected locally and found to drain specifically into the left metastatic popliteal LN. MR/Optical/NIR fluorescence images of the left metastatic popliteal LN were acquired, and PTT was applied.

Abbreviations: LN, lymph node; MRI, magnetic resonance imaging; FL, fluorescent; PTT, photothermal therapy.

Preparation and Characterization of cRGD-PPIG NPs

First, PDA NPs were synthesized via oxidation polymerization in an alkaline environment. To improve their solubility in PBS, PDA NPs were modified with PEG. Measurements of particle stability using PDA NPs, PPIG NPs, and cRGD-PPIG NPs of different sizes at 0, 1, 6, 12, and 24 h are summarized in Supplementary Figure S1. PPIG NPs and cRGD-PPIG NPs remained stable in PBS after 24 h, whereas PDA NPs had precipitated. These results confirmed the improved stability of PDA NPs upon PEG modification. To load cRGD on PEG-PDA NPs, EDC (50 mg) and sulfo-NHS (30 mg) were added to a solution containing PEG-PDA NPs (15 mg) and the mixture was stirred at room temperature for 4 h. The mixture was then washed with PBS to remove excess EDC and sulfo-NHS. Next, NH_2-cRGD (2 mg) was added to the mixture, and the reaction was proceeded at 4 °C for 10 h with continuous stirring. After washing and centrifugation, the MRI contrast ($Gd(NH_2)_2$) and NIR dye (IR820) were loaded on cRGD-PEG-PDA NPs. The resulting cRGD-PPIG NPs were characterized using TEM, DLS, zeta potential measurement, nuclear magnetic resonance (NMR) spectroscopy, and UV-vis spectral analysis. TEM and DLS confirmed that the synthesized cRGD-PPIG NPs were 79.2 ± 31.6 nm in diameter (Figure 1A and B) and had a zeta potential of −42.5 ± 8.3 eV (Figure 1C). Evaluation by ^{1}H NMR revealed a specific peak for cRGD peptides (Figure 1D, blue box).[32] Together, these results indicated the successful loading of cRGD peptides on the NPs.

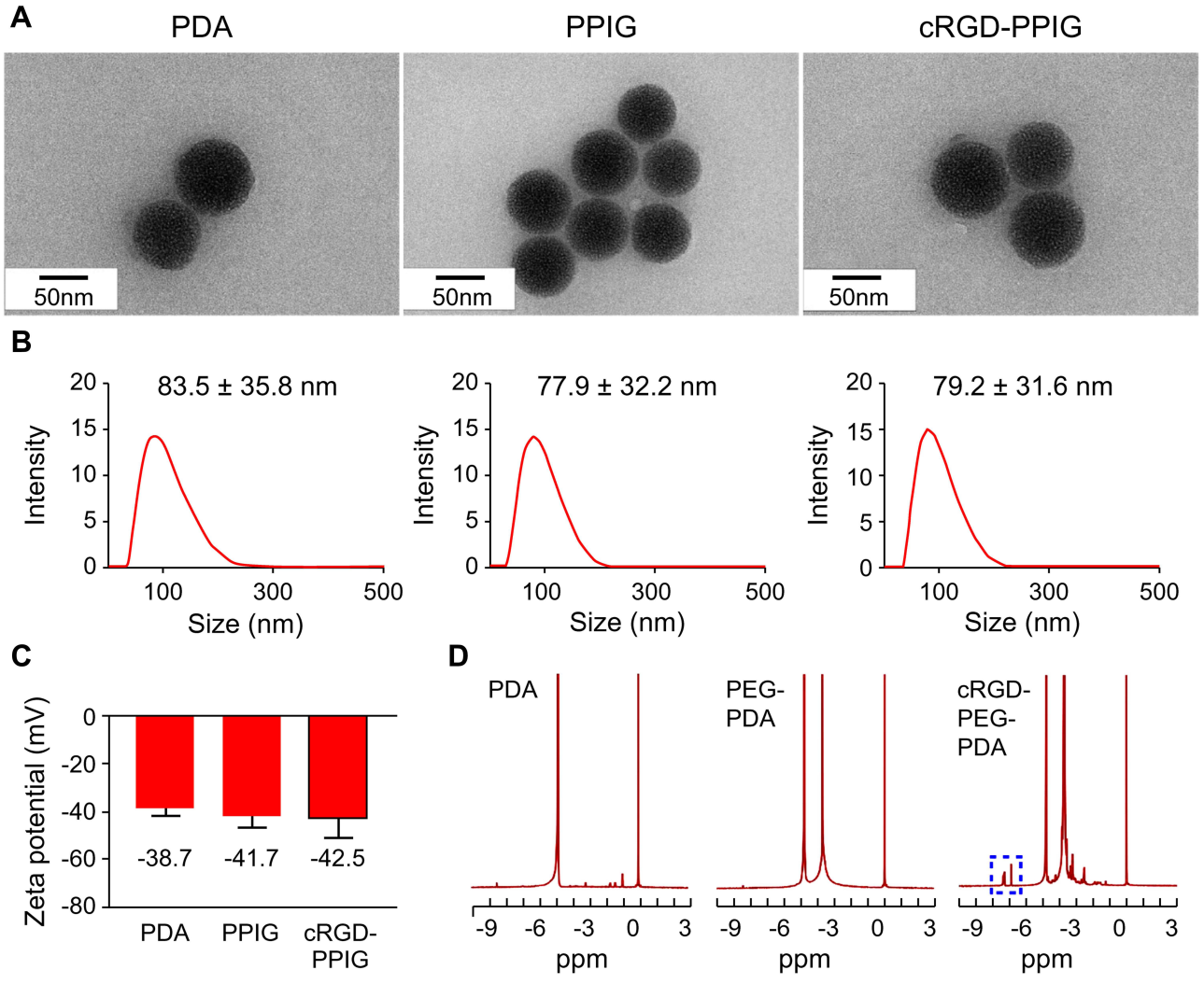

Figure 1 In vitro characterization of multi-sized PDA NPs, PPIG NPs, and cRGD-PPIG NPs. (**A**) TEM images. (**B**) DLS results. (**C**) Zeta potentials. (**D**) ^{1}H NMR spectroscopy results.

Abbreviations: PPIG, PEG-PDA@IR820/$Gd(NH_2)_2$; TEM, transmission electron microscope; DLS, dynamic light scattering; NMR, nuclear magnetic resonance.

NIR imaging and photothermal performance of cRGD-PPIG NPs were evaluated. The broadband UV-vis absorption spectra of cRGD-PPIG NPs are shown in Figure 2A. A distinctive absorbance peak was detected at ~820 nm owing to IR820 loading. In the MRI performance evaluation, the cRGD-PPIG NPs became brighter with increasing NP concentration. A linear relationship can be identified in Figure 2B. The temperature of laser-exposed cRGD-PPI NP solutions increased with increasing NP concentration and laser power density (Figure 2C–F). The temperature of the cRGD-PPIG NP solution (400 μg/mL) reached 38.6 °C ± 2.3 °C rapidly at a power density of 1 W/cm^2 after which the temperature increased further. The thermal image became brighter as the NP concentration or laser power density increased. The photothermal effect of cRGD-PPIG NPs was stable over five irradiation cycles (Figure 2E). These results indicate that cRGD-PPIG NPs are effective PTT agents.

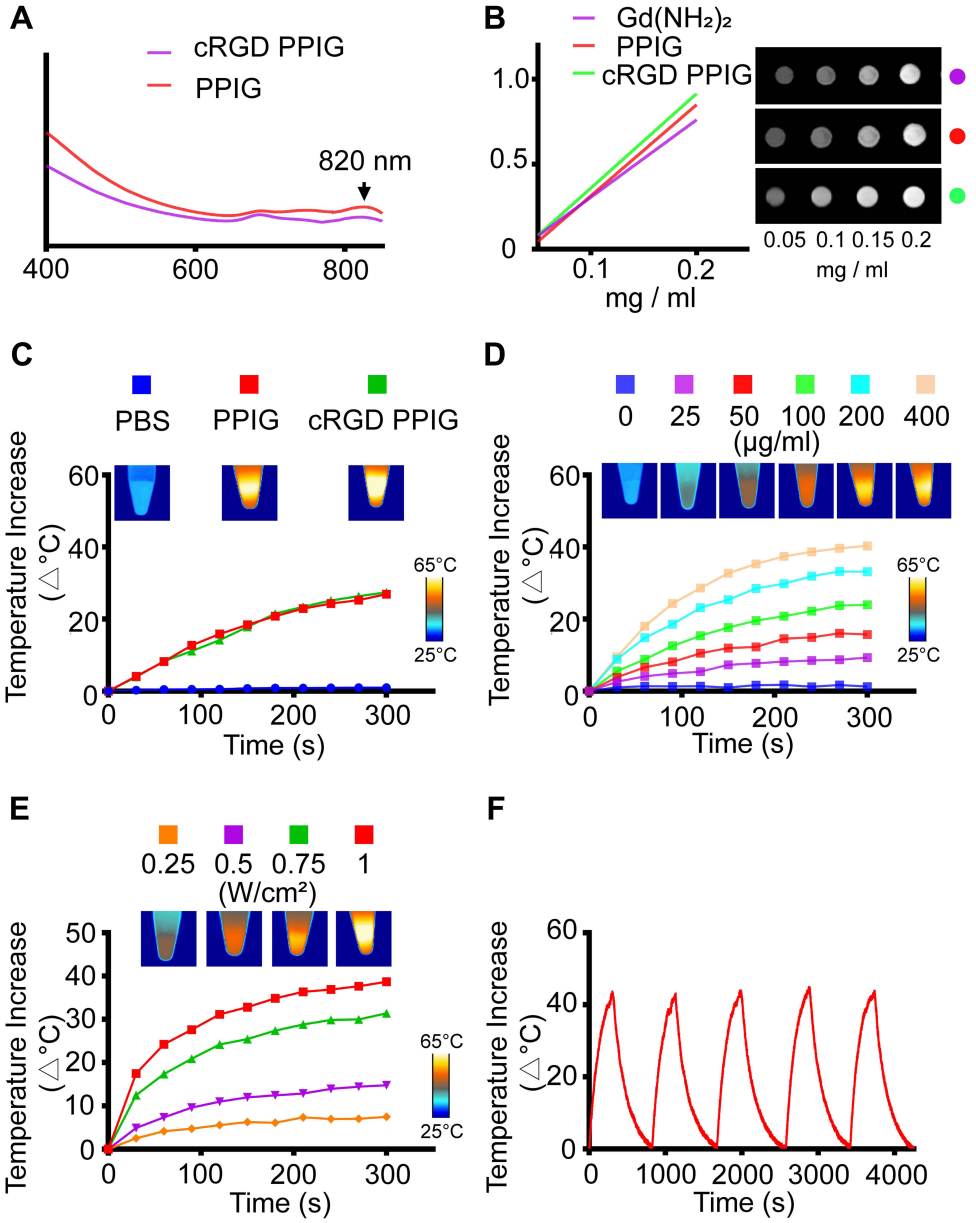

Figure 2 In vitro characterization of cRGD-PPIG NPs. (**A**) UV-vis-NIR spectra of PPIG NPs and cRGD-PPIG NPs. (**B**) Relative MR signal intensities of cRGD-PPIG NPs at various concentrations. (**C**) Temperature changes and thermal images of solutions containing PPIG NPs and cRGD-PPIG NPs (200 μg/mL) in PBS under 808 nm laser irradiation (1 W/cm²) for 5 min. PBS alone was used as the negative control. (**D**) Temperature changes and thermal images of solutions containing different concentrations of cRGD-PPIG NPs (0, 25, 50, 100, 200, and 400 μg/mL) in PBS under 808 nm laser irradiation (1 W/cm²) for 5 min. (**E**) Temperature changes and thermal images of solutions containing cRGD-PPIG and PPIG NPs (200 μg/mL) under 808 nm laser irradiation at various power densities (0.0.25, 0.375, 0.5, and 1 W/cm²). (**F**) Temperature pattern of a solution containing cRGD-PPIG NPs (400 μg/mL) in PBS over five cycles of NIR laser irradiation (808 nm, 1 W/cm²).

Biosafety and Cellular Uptake of cRGD-PPIG NPs in vitro

Melanin and its analogs have been shown to possess strong biocompatibility, making them widely used as drug delivery platforms.[21] Previously, we identified PDA as another highly biocompatible molecule.[33] To assess the biocompatibility of the cRGD-PPIG NPs generated in the present study, we used the CCK-8 assay. Biosafety measurements of PPIG NPs and cRGD-PPIG NPs in normal SVEC4-10 cells revealed viability above 85% (Figure 3A). Therefore, we hypothesized that both PPIG NPs and cRGD-PPIG NPs were safe for use as drug delivery systems in biomedical applications.

Integrin $\alpha_v\beta3$ is specifically overexpressed on cancer cell membranes. Because the cRGD peptide targets integrin $\alpha_v\beta3$,[34–36] cRGD-conjugated NPs were expected to have a higher affinity for tumor cells. For this purpose, MKN45 cells were selected as in vitro models because the integrin $\alpha_v\beta3$ was significantly upregulated in these cells compared with GES-1 cells (Supplementary Figure S2). To confirm the synergistic uptake of cRGD-PPIG NPs, MKN45 cells were exposed separately to PPIG NPs and cRGD-PPIG NPs for 4 h and then analyzed using flow cytometry and CLSM. Using flow cytometry to assess the accumulation of IR820 in MKN45 cells, we found that the uptake of IR820 at 24 h was three times higher following treatment with cRGD-PPIG NPs compared to PPIG NPs (Figure 3B). Consequently, according to the CLSM results, the red fluorescence intensity of IR820 increased in both PPIG and cRGD-PPIG groups (Figure 3C), although it was stronger in the latter (Figure 3D), indicating that cRGD helped increase the cell uptake ratio after binding to the highly expressed integrin $\alpha_v\beta3$ receptor in MKN45 cells.

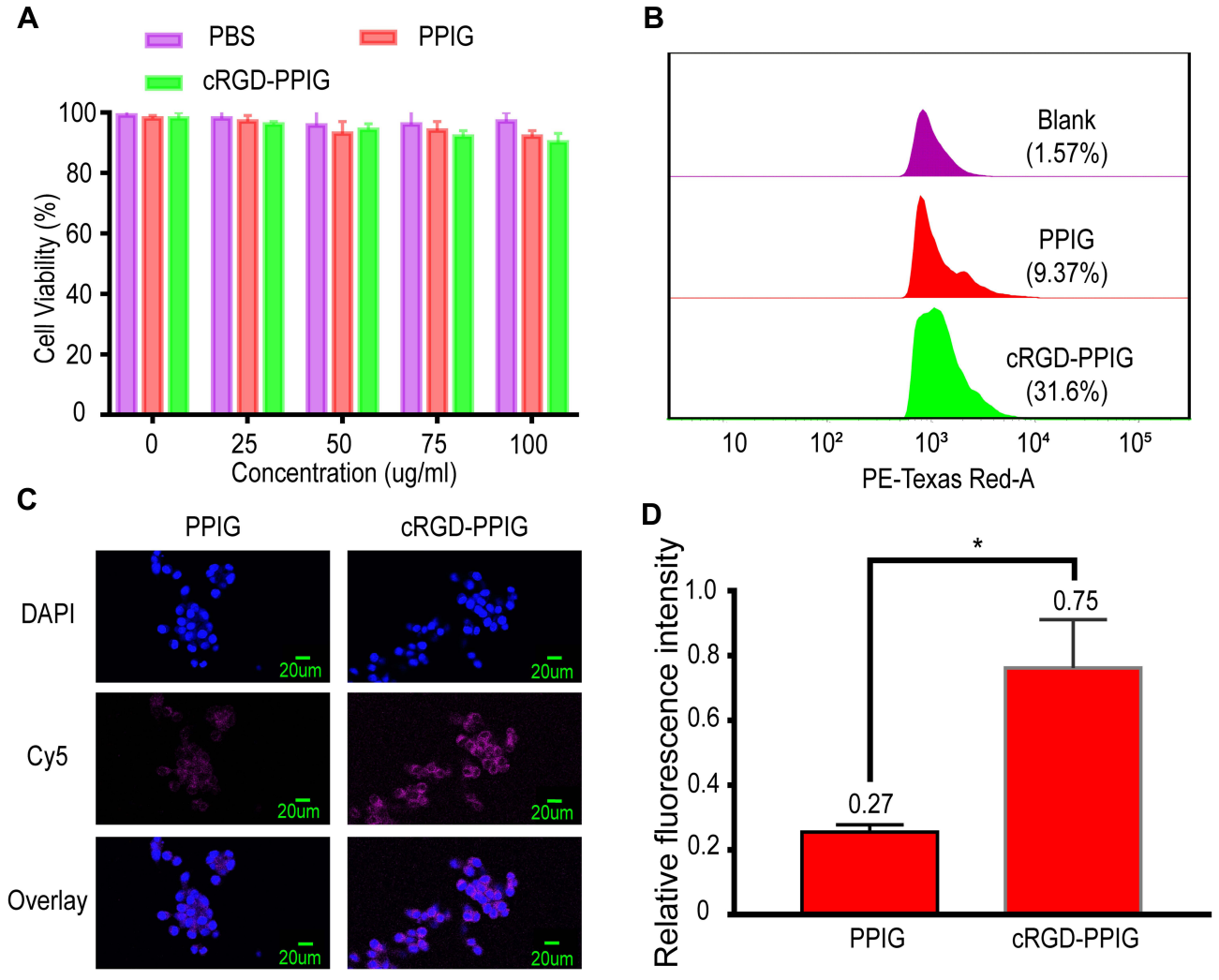

Figure 3 In vitro biosafety and cell uptake of cRGD-PPIG NPs. (**A**) Viability of SVEC4-10 cells incubated with PBS (control), PPIG NPs, and cRGD-PPIG NPs at different concentrations (0, 25, 50, 75 and 100 μg/mL). (**B**) Flow cytometry analysis of MKN45 cells incubated with PBS (blank), PPIG NPs, and cRGD-PPIG NPs. (**C**) CLSM of MKN45 cells incubated with PPIG NPs and cRGD-PPIG NPs. Images were acquired in the Cy5.5 channel (670 nm) and DAPI channel (358 nm). (**D**) Relative fluorescence intensity of MKN45 cells incubated with PPIG NPs and cRGD-PPIG NPs. *$p < 0.05$.

cRGD-PPIG NPs Have a Combined PTT/Photodynamic Therapy (PDT) Effect on Gastric Cancer Cells

PDA NPs are potential PTT/PDT agents with intrinsic NIR-responsive properties.[33] IR820 was previously reported to be a promising NIR dye for PTT and PDT.[37] Here, we hypothesized that combining cRGD-PPIG NPs with NIR irradiation could cause oxidative stress with combined PTT and PDT effects. To test the synergistic PTT/PDT effect of these NPs, MKN45 cells were incubated with cRGD-PPIG NPs at different concentrations. The MKN45 cells were then subjected or not to NIR irradiation (1 W/cm^2, 5 min). After culturing for 24 h, treated MKN45 cells were analyzed using CCK-8 and EdU staining kits. No significant change in cell viability was observed with increasing concentrations of PPIG NPs, cRGD-PPIG NPs, or NIR irradiation alone compared to the control (Figure 4A). However, combinations of PPIG NPs + NIR irradiation and cRGD-PPIG NPs + NIR irradiation achieved a desirable therapeutic effect, with the latter causing the highest rate of gastric cancer cell death. NIR-irradiated and either PPIG NP-treated or cRGD-PPIG NP-treated cells showed fewer EdU-positive cells than the control or cells treated with only PPIG NPs, cRGD-PPIG NPs, and NIR (Figure 4B and D).

High levels of intracellular ROS can damage mitochondria and cause apoptosis. Emerging evidence indicates that the NIR-mediated phototherapeutic effect can activate the endogenous oxidative stress signaling pathway, promoting intracellular ROS production.[38,39] To clarify whether cRGD-PPIG NPs could exert a PDT effect, treated MKN45 cells were analyzed using a dichloro-dihydro-fluorescein diacetate probe to quantify intracellular ROS. CLSM revealed no significant ROS changes in the PPIG, cRGD-PPIG, or NIR-only irradiation groups compared to the control. Interestingly, ROS generation was significantly increased in cells treated with PPIG NPs + NIR. Overall, MKN45 cells treated with cRGD-PPIG NPs + NIR exhibited the highest ROS production and, hence, cytotoxic effect (Figure 4C and E). Collectively, these findings suggest that cRGD-PPIG NPs promote PTT and PDT effects against MKN45 cells.

In vivo Tumor-Targeted Multimodal LN Mapping Using cRGD-PPIG NPs

MRI has proven valuable in the preoperative GC Tumour Node Metastasis classification.[40] However, its low accuracy for N staging, ranging from 52.17% to 71%, hampers its clinical application in GC diagnoses.[41–44] Intravenous MRI contrast agents may not be suitable for MRI detection of LNs because of their relatively small size. However, indirect magnetic resonance lymphangiography (MR-LAG), in which MRI contrast agents are injected peritumorally, might be valuable for identifying nodal micrometastases or high-risk nodal regions. Indirect MR-LAG explains local lymphatic drainage with a high-resolution MRI. Thus, this technique has been used to characterize cervical LNs in patients with head and neck cancer.[45] Current MRI agents cannot differentiate metastatic LNs because of their lack of tumor-targeting ability.[46] In the present study, we investigated the tumor-targeted metastatic LN mapping ability of cRGD-PPIG NPs in a mouse model bearing an MKN-45 tumor using indirect MR-LAG. Proper volume samples (50 μL containing 50 μg of cRGD-PPIG or PPIG NPs per mouse) were injected into the left rear footpad of nude mice bearing MKN45 tumors (n = 3/group). Thereafter, mice were anesthetized, and cRGD-PPIG and PPIG NP accumulation in the metastatic LN and normal LN were investigated using MRI before and at 1, 2, and 4 h after injection (Figure 5). The relative intensity of the MR signal in LN is shown in Supplementary Figure S3. At 1 h post-injection, popliteal LN was visualized in all groups. The cRGD-PPIG NP metastatic LN group displayed the highest MR signal intensity and remained high for 4 h after injection. For the PPIG NP metastatic LN group, lower signal intensity was observed relative to that of the cRGD-PPIG NP metastatic LN group. For the cRGD-PPIG NPs and PPIG NP normal LN groups, the lowest MR signal intensity was observed after injection. Therefore, by using cRGD-PPIG NPs, we might achieve targeted indirect MR-LAG.

Optical LN mapping is convenient because of its ease of use and reliance on readily accessible equipment. Nanocarbon NPs have been applied in clinical settings owing to their natural black color, which is easy to detect. If properly sized, nanocarbon NPs could specifically enter lymphatic vessels and stain LNs rather than traverse blood endothelial cell junctions.[47–49] However, the lack of multimodal LN mapping and targeting of specific pathological outcomes, including inflammation, fibrosis, and tumorigenesis, has limited the application of nanocarbon NPs in clinical diagnosis and therapy.[50] In the present study, we used cRGD-PPIG NPs to overcome the limitations of nanocarbon NPs. After cRGD-PPIG NPs and PPIG NPs were injected locally into mice, the animals were sacrificed for optical imaging (Figure 6). In the cRGD-PPIG group, metastatic LNs were stained 1 h

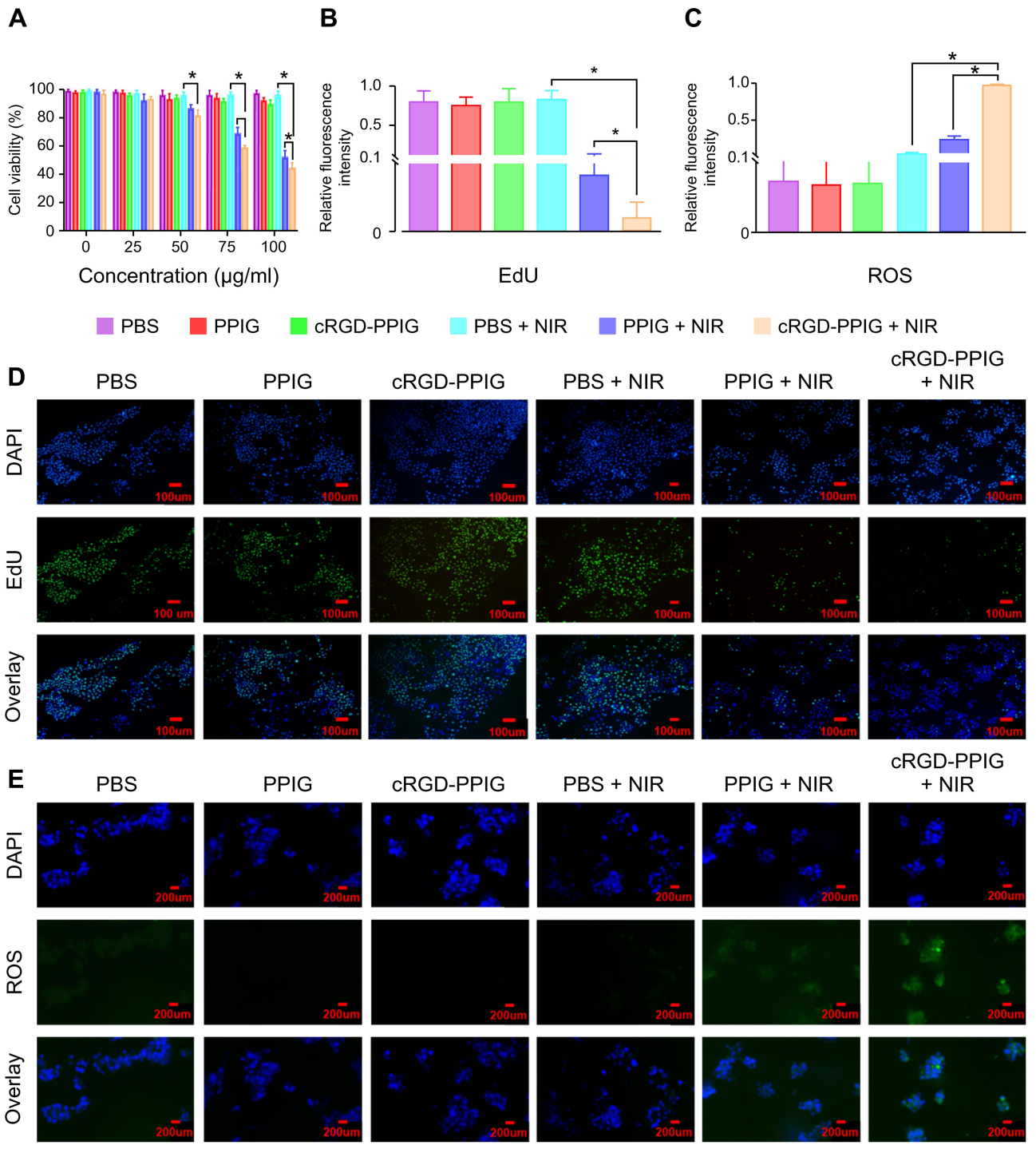

Figure 4 In vitro PTT and PDT effect of cRGD-PPIG NPs on gastric cancer cells. (**A**) Viability of MKN45 cells incubated with PBS (control), PPIG NPs, and cRGD-PPIG NPs at various concentrations and subjected or not to 808 nm irradiation (1 W/cm^2). The values were calculated using a CCK-8 kit. (**B**) Relative fluorescence intensity of MKN45 cells incubated with PBS, PPIG NPs, and cRGD-PPIG NPs at various concentrations and subjected or not to NIR irradiation. Values were calculated based on EdU staining. (**C**) Relative fluorescence intensity of MKN45 cells incubated with PBS, PPIG NPs, and cRGD-PPIG NPs at various concentrations and subjected or not to NIR irradiation. Values were calculated based on ROS staining. *$p < 0.05$. (**D**) Representative images of EdU-stained MKN45 cells incubated with PBS, PPIG NPs, and cRGD-PPIG NPs at various concentrations and subjected or not to NIR irradiation. (**E**) Representative images of ROS-stained MKN45 cells incubated with PBS, PPIG NPs, and cRGD-PPIG NPs and subjected or not to NIR irradiation (1 W/cm^2).

after injection and the staining persisted for 4 h. A relatively weaker coloration of LNs was observed when metastatic LNs were stained with PPIG NPs or when non-metastatic LNs were stained with cRGD-PPIG NPs and PPIG NPs. These results show that cRGD-PPIG NPs aided tumor-targeted LN optical imaging.

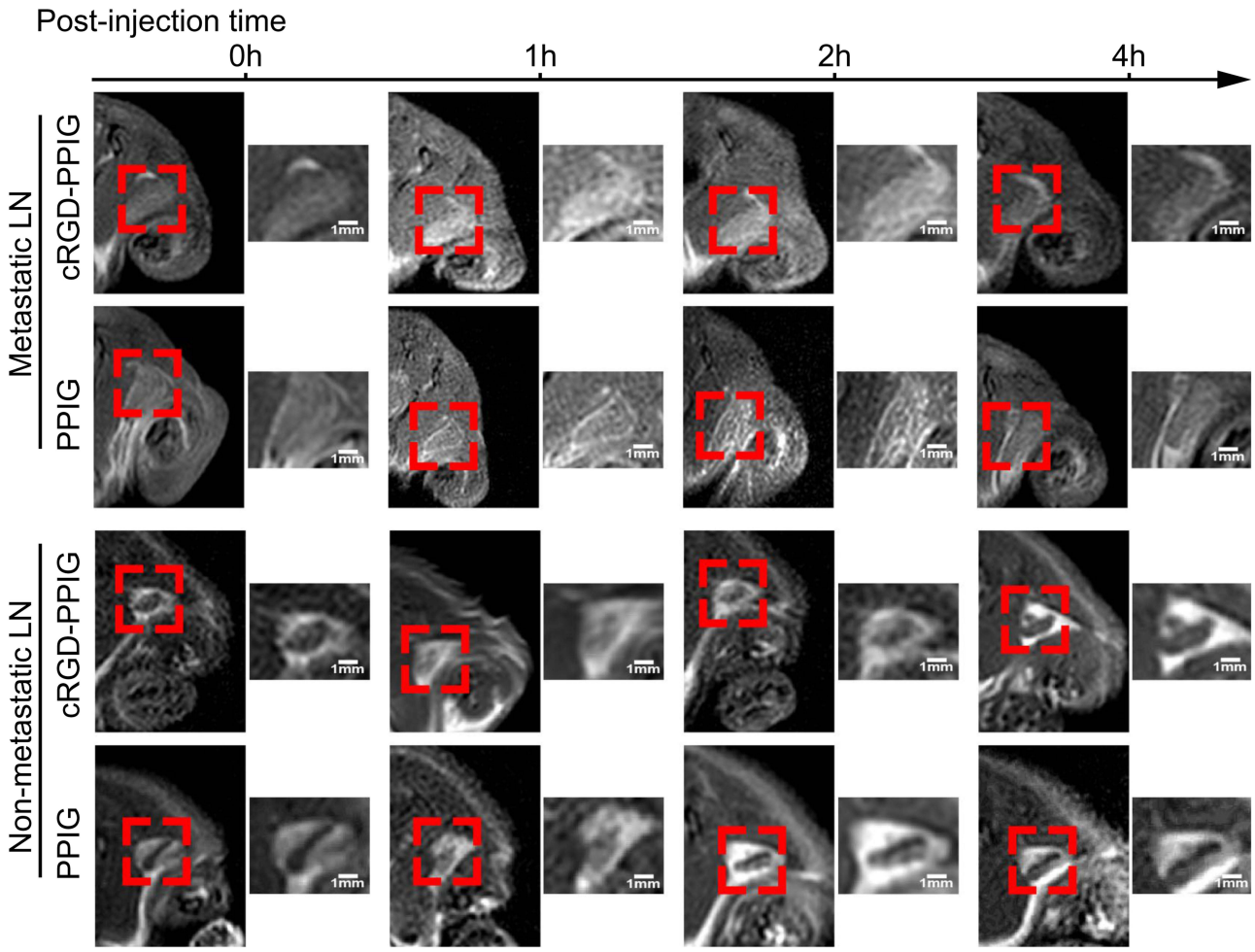

Figure 5 In vivo mouse LN MR imaging using cRGD-PPIG NPs and PPIG NPs. In vivo MR images of mouse LNs before and at 1, 2, and 4 h after injection of the cRGD-PPIG NPs and PPIG NPs. The red boxes indicate the LNs.

Recent scientific and technological developments have brought increasing attention to NIR fluorescent dyes because of their optimal tissue penetration in biological samples, low light scattering, and ability to stain both LNs and the lymphatic route.[14] Despite these advantages, the actual application of NIR fluorescent dyes in clinical practice remains limited. Some clinical studies have associated LN detection using indocyanine green with a high rate of false-negative results.[6,51–53] This could be attributed to the lack of multimodal LN mapping ability of this dye. Moreover, nonspecific NIR fluorescence dyes may not accurately map metastatic LNs during surgery. Here, we used cRGD-PPIG NPs to achieve tumor-targeted LN NIR fluorescence imaging. The LN mapping ability of cRGD-PPIG NPs and PPIG NPs in LNs was also explored. Briefly, equal amounts of cRGD-PPIG NPs and PPIG NPs were injected locally followed by NIR fluorescence LN imaging before and 1, 2, and 4 h after injection (Figure 7). The NIR fluorescence intensity of LNs was also measured (Supplementary Figure S4). Similar to the optical imaging results, the cRGD-PPIG metastatic LN group attained the highest NIR fluorescence intensity 1 h after injection, and the signal intensity lasted for 4 h. In the other groups, NIR fluorescence intensities were relatively weak. Multimodal LN mapping agents such as cRGD-PPIG NPs show strong clinical application potential as tumor-targeting therapeutics.

cRGD-PPIG NPs Could Inhibit the Growth of Metastatic LNs in vivo

PTT has emerged as an effective therapeutic method against solid tumors. By using NIR light-absorbing agents under 808 nm laser irradiation, PTT can raise the local tumor temperature, causing irreversible cell death to neoplastic tissues

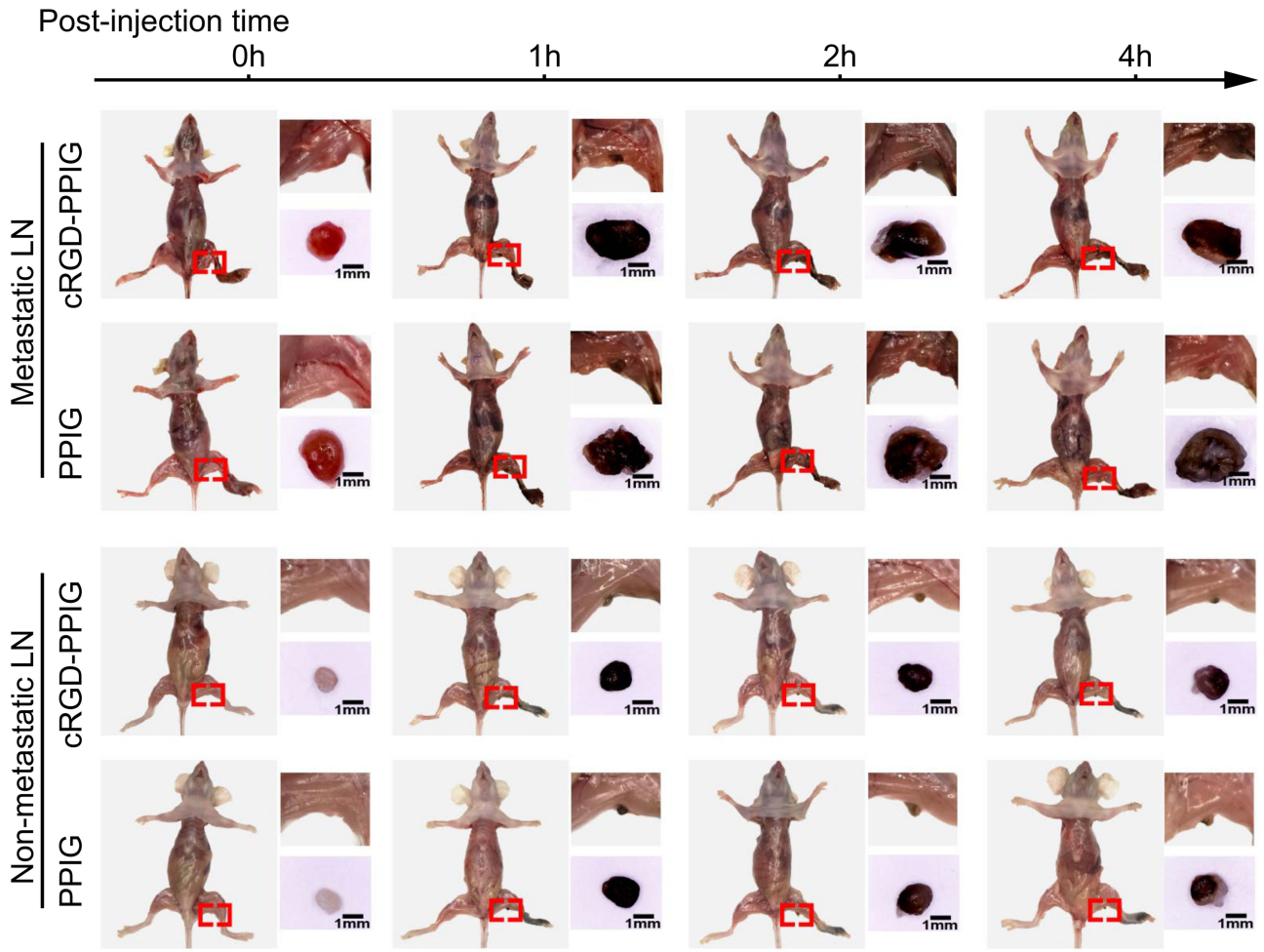

Figure 6 In vivo mouse LN optical imaging using PPIG NPs and cRGD-PPIG NPs. Red boxes indicate metastatic or non-metastatic LNs. Higher-magnification images of the boxed areas and the LN after resection are presented to the right of each mouse image.

while sparing healthy tissues from unnecessary damage.[54,55] Therefore, PTT has been investigated as an alternative to surgical resection of metastatic LNs.[56,57]

The in vivo biodistribution of cRGD-PPIG NPs revealed good fluorescence and optical imaging, as well as thermal capacity toward metastatic LNs. Guided by multimodal LN imaging, the phototherapeutic efficacy of cRGD-PPIG NPs was further evaluated in MKN45 tumor-bearing mice. One hour after peritumoral PBS injection (control group), PPIG NPs, or cRGD-PPIG NPs, metastatic LNs were irradiated at 1 W/cm^2 with an 808 nm laser for 5 min. Subsequently, in vivo images were captured with an infrared thermal camera. As shown in Figure 8A, the tumor temperature of the metastatic LNs in the cRGD-PPIG + NIR group increased from ~32 °C to ~55 °C within 3 min and was then maintained at ~55 °C to 57 °C for the next 2 min to ensure sufficient PTT effect. This temperature was markedly higher than that observed in the PPIG + NIR group (approximately 51 °C) and the control group (approximately 39 °C) (Figure 8B). Therefore, our results demonstrate that cRGD-PPIG NPs can remarkably raise the temperature during PTT.

To further analyze the antitumor effect of cRGD-PPIG NPs on metastatic LNs in vivo, we randomly divided the mice into six groups and treated them with PBS (negative control), PBS + NIR, PPIG NPs, PPIG NPs + NIR, cRGD-PPIG NPs, or cRGD-PPIG NPs + NIR. Ten days after treatment, the morphology of metastatic LNs was similar among the PBS, PBS + NIR, PPIG, and cRGD-PPIG groups. In contrast, the tumor growth rates in the PPIG + NIR and cRGD-PPIG + NIR groups were approximately 60% and 80% lower, respectively, compared to the control group (Figure 8C). The cRGD-PPIG + NIR group showed the most significant weight loss, whereas no significant differences were observed among the PBS, PBS + NIR, PPIG, and cRGD-PPIG groups (Figure 8D).

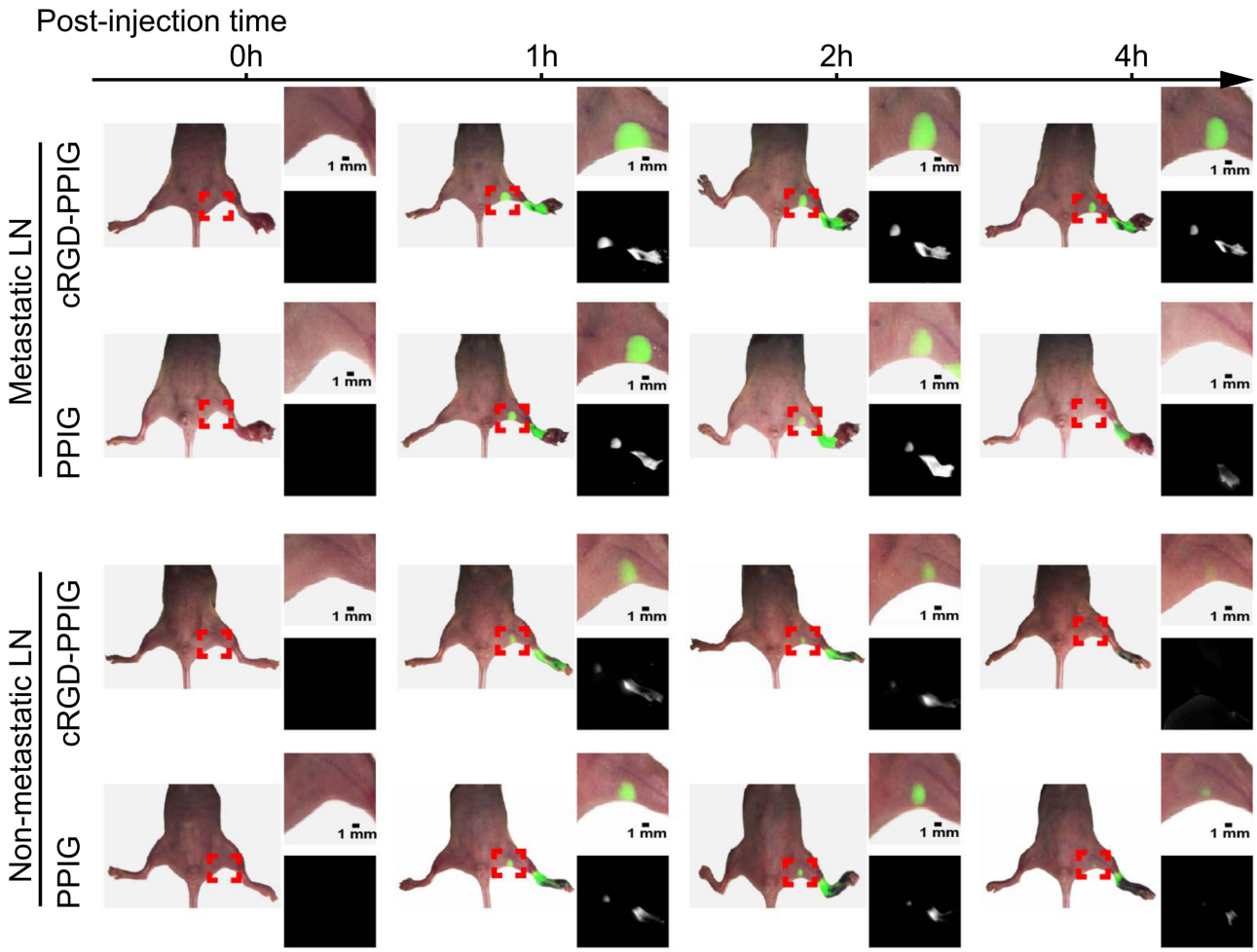

Figure 7 In vivo mouse LN NIR fluorescence imaging of PPIG NPs and cRGD-PPIG NPs. Images were taken before and at 1, 2, and 4 h after local injection of PPIG NPs and cRGD-PPIG NPs. Red boxes indicate the LNs. Higher-magnification images of the boxed areas are presented as upper right inserts, whereas black and white images of the fluorescence signal are presented as lower right inserts.

Isolated metastatic LNs were subjected to immunofluorescence staining. TUNEL is a classic marker of DNA fragmentation in apoptotic tumor cells. Immunofluorescence revealed significantly stronger TUNEL staining in the cRGD-PPIG + NIR group (Figure 8E). Consequently, in vivo PTT consistently highlighted the superiority of cRGD-PPIG NPs in inhibiting metastatic LN growth through PTT and PDT effects.

In vivo Biodistribution and Biosafety of cRGD-PPIG NPs

Finally, we injected cRGD-PPIG and PPIG NPs locally into nude mice to evaluate their biodistribution during LN mapping. At 1 h after injection (corresponding to the highest NIR fluorescence signal), mice were sacrificed via an overdose of pentobarbital, and the major organs, including the heart, liver, spleen, lungs, kidneys, brain, and LNs, were excised for imaging (Supplementary Figure S5A). NIR fluorescence images indicate that cRGD-PPIG NPs accumulated mainly in LNs, whereas only a small amount of NIR fluorescence was observed in the liver and kidneys. Histological examination revealed no apparent histopathological damage in the major organs of animals treated with PPIG NPs (Supplementary Figure S5B). Furthermore, brown-yellow NPs were observed in the metastatic LNs. These findings demonstrate that cRGD-PPIG NPs are retained in LNs.

To evaluate the biosafety of cRGD-PPIG NPs in vivo, we measured blood biochemical indices, including blood urea nitrogen and creatinine for kidney function, and alanine transaminase and aspartate transaminase for liver function.[56,58]

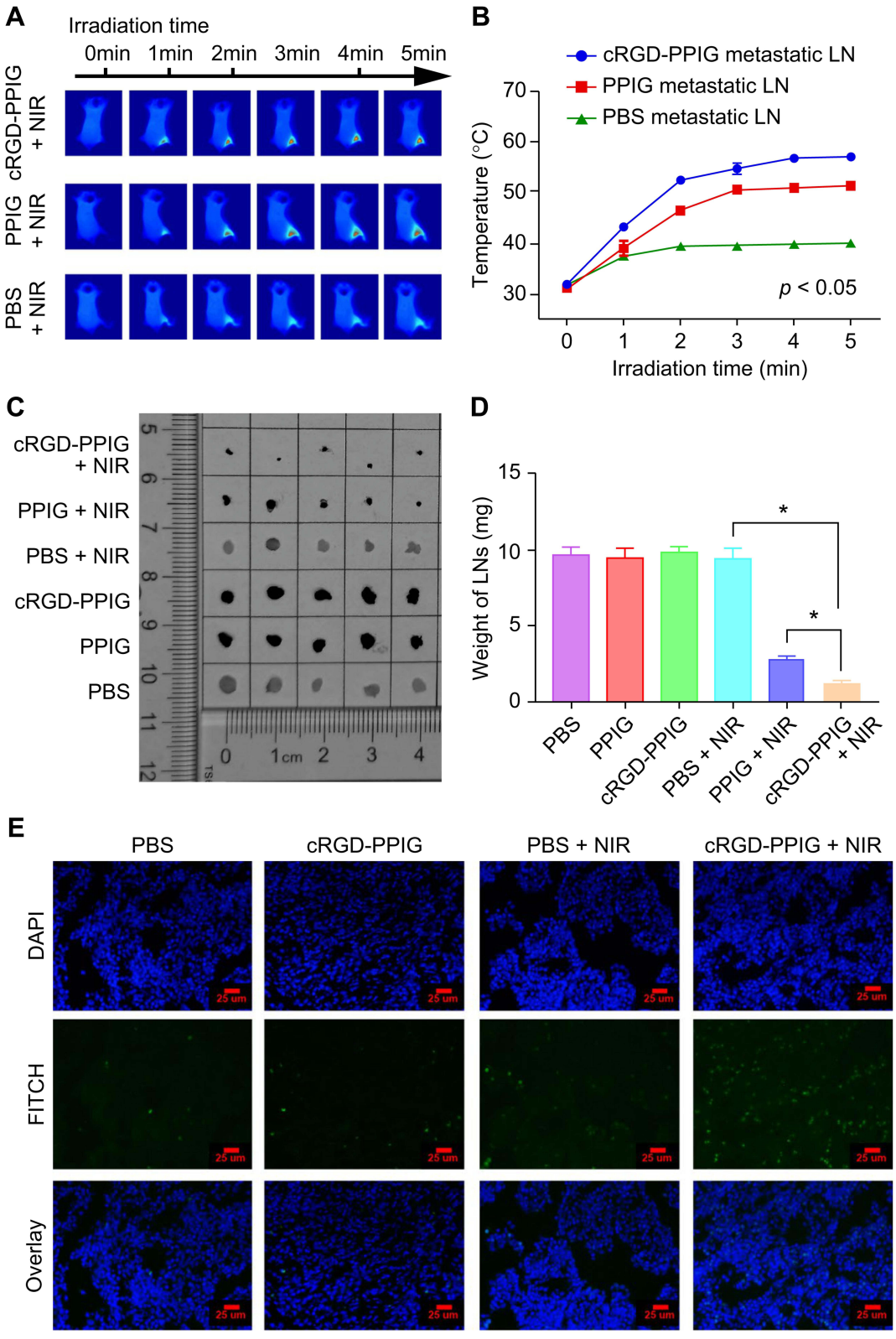

Figure 8 In vivo photothermal treatment of LNs in mice. (**A**) Representative thermal images of mice treated with PBS, PPIG NPs, and cRGD-PPIG NPs under irradiation at 1 W/cm² with an 808 nm laser. (**B**) Temperature change in metastatic LNs treated with PBS, PPIG NPs, or cRGD-PPIG NPs under irradiation at 1 W/cm² with an 808 nm laser. (**C**) Images of non-metastatic LNs and metastatic LNs collected from mice 10 days after the indicated treatment. (**D**) Average weights of LNs from Figure 7C. *$p < 0.05$. Error bars represent the standard deviations (n = 5). (**E**) TUNEL staining of metastatic LN tissue slices collected from mice on day 3 after various treatments.

No significant differences were observed in the indices in treated versus untreated rats over 1 month (Supplementary Figure S6). These findings suggest that PPIG NPs exert no noticeable toxicity on liver and kidney function.

Conclusion

In this study, a cRGD-PPIG NP tumor-targeted LN mapping agent was successfully developed. The generated cRGD-PPIG NPs facilitated MR/optical/NIR fluorescence multimodal targeted mapping of gastric cancer metastatic LNs. Furthermore, accurate guided PTT was achieved by locally injecting cRGD-PPIG NPs. The loaded cRGD ligand on the surface of NPs was selectively taken up by cancerous MKN45 cells overexpressing integrin $\alpha_v\beta3$. Importantly, cRGD-PPIG NPs specifically targeted metastatic MKN45 LNs, enabling MR/optical/NIR fluorescence multimodal gastric cancer metastatic LN mapping and PTT in vivo. Accordingly, the proposed NPs represent an alternative to surgical resection of LN metastases. Future studies on the long-term toxicology of cRGD-PPIG NPs in vivo would explain the potential clinical applications of these antitumor agents.

Abbreviations

CLSM, confocal laser scanning microscopy; cRGD, circular-arginine-glycine-aspartic acid sequence; DLS, dynamic light scattering; EDC, ethylcarbodiimide hydrochloride; LN, lymph node; MRI, magnetic resonance imaging; MR-LAG, magnetic resonance lymphangiography; NIR, near-infrared; NMR, nuclear magnetic resonance; NP, nanoparticle; PDA, polydopamine; PEG, polyethylene glycol; PPIG, PEG-PDA@IR820/Gd$(NH_2)_2$; PPT, photothermal therapy; TEM, transmission electron microscopy.

Acknowledgments

The authors would like to thank Dr. Bingquan Lin, Dr. Bingxia Zhao, and Dr. Peng Zhao from Southern Medical University for providing technical support. We would also like to thank Editage for English language editing. This research was funded by the National Natural Science Foundation of China (grant numbers 82001948 and 81971746); the Natural Science Foundation of Guangdong Province, China (grant number 2017A030306023); the Guangdong Provincial Key Laboratory of Precision Medicine for Gastrointestinal Cancer (grant number 2020B121201004); the Guangdong Provincial Major Talents Project (grant number 2019JC05Y361); the Outstanding Youths Development Scheme of Nanfang Hospital, Southern Medical University (grant number 2017J006); the Medical Scientific Research Foundation of Guangdong Province of China (grant number A2020297); President Foundation of Nanfang Hospital, Southern Medical University (grant number 2021C041); the Special Funds for Cultivation of Guangdong College Students' Scientific and Technological Innovation (grant numbers pdjh2020a0108, pdjh2020a0106, and pdjh2020a0109); and the College Students' Innovative Entrepreneurial Training Plan Program (grant numbers S202012121020 and 595 S202012121051).

Disclosure

The authors report no conflicts of interest in this work.

References

1. Fitzmaurice C, Abate D, Abbasi N.; Global Burden of Disease Cancer Collaboration, Fitzmaurice C, Abate D, et al. Global, regional, and national cancer incidence, mortality, years of life lost, years lived with disability, and disability-adjusted life-years for 29 cancer groups, 1990 to 2017: a systematic analysis for the global burden of disease study [published correction appears in JAMA Oncol. 2020 Mar 1; 6(3):444][published correction appears in JAMA Oncol. 2020 May 1; 6(5):789][published correction appears in JAMA Oncol. 2021 Mar 1;7(3):466]. *JAMA Oncol*. 2019;5 (12):1749–1768. doi:10.1001/jamaoncol.2019.2996
2. Telli ML, Gradishar WJ, Ward JH. NCCN guidelines updates: breast cancer. *J Natl Compr Canc Netw*. 2019;17(5.5):552–555. doi:10.6004/jnccn.2019.5006
3. Qiu H, Zhou Z. [Updates and interpretation on NCCN clinical practice guidelines for gastric cancer 2017 version 5]. *Chinese Journal of Gastrointestinal Surgery*. 2018;21(2):160–164. Chinese.
4. Mehralivand S, van der Poel H, Winter A, Choyke PL, Pinto PA, Turkbey B. Sentinel lymph node imaging in urologic oncology. *Transl Androl Urol*. 2018;7(5):887–902. doi:10.21037/tau.2018.08.23
5. Dumitru D, Khan A, Catanuto G, Rocco N, Nava MB, Benson JR. Axillary surgery in breast cancer: the beginning of the end. *Minerva Chir*. 2018;73(3):314–321. doi:10.23736/S0026-4733.18.07728-3

6. Kwon IG, Son T, Kim HI, Hyung WJ. Fluorescent lymphography-guided lymphadenectomy during robotic radical gastrectomy for gastric cancer. *JAMA Surg*. 2019;154(2):150–158. doi:10.1001/jamasurg.2018.4267
7. Wu XN, Liu CQ, Tian JY, Guo MF, Xu MQ. Prognostic significance of the number of lymph nodes examined in node-negative Siewert type II esophagogastric junction adenocarcinoma. *Int J Surg*. 2017;41:6–11. doi:10.1016/j.ijsu.2017.03.028
8. Gao P, Song YX, Wang ZN, et al. Integrated ratio of metastatic to examined lymph nodes and number of metastatic lymph nodes into the AJCC staging system for colon cancer. *PLoS One*. 2012;7(4):e35021. doi:10.1371/journal.pone.0035021
9. Gu L, Chen B, Shen Z, et al. The relationship between the number of examined lymph nodes and the efficacy of chemotherapy for gastric cancer. *Surg Today*. 2020;50(6):585–596. doi:10.1007/s00595-019-01925-3
10. Colen RR, Vangel M, Wang J, et al. Imaging genomic mapping of an invasive MRI phenotype predicts patient outcome and metabolic dysfunction: a TCGA glioma phenotype research group project. *BMC Med Genomics*. 2014;7(1):30. doi:10.1186/1755-8794-7-30
11. Sutton EJ, Braunstein LZ, El-Tamer MB, et al. Accuracy of magnetic resonance imaging-guided biopsy to verify breast cancer pathologic complete response after neoadjuvant chemotherapy: a nonrandomized controlled trial. *JAMA Netw Open*. 2021;4(1):e2034045. doi:10.1001/jamanetworkopen.2020.34045
12. Giganti F, De Cobelli F, Canevari C, et al. Response to chemotherapy in gastric adenocarcinoma with diffusion-weighted MRI and (18) F-FDG-PET/CT: correlation of apparent diffusion coefficient and partial volume corrected standardized uptake value with histological tumor regression grade. *J Magn Reson Imaging*. 2014;40(5):1147–1157. doi:10.1002/jmri.24464
13. Yoshida K, Ohta K, Ohhashi I, Nakajima T, Takagi K, Nishi M. [Studies on gastric lymphatics by using activated carbon particle (CH44) and lymph node metastasis of gastric cancer]. Journal of Japan Surgical Association. 1988;89(5):664–670. in Japanese.
14. Escobedo JO, Rusin O, Lim S, Strongin RM. NIR dyes for bioimaging applications. *Curr Opin Chem Biol*. 2010;14(1):64–70. doi:10.1016/j.cbpa.2009.10.022
15. Woods RW, Camp MS, Durr NJ, Harvey SC. A Review of options for localization of axillary lymph nodes in the treatment of invasive breast cancer. *Acad Radiol*. 2019;26(6):805–819. doi:10.1016/j.acra.2018.07.002
16. Li J, Deng X, Wang L, Liu J, Xu K. Clinical application of carbon nanoparticles in lymphatic mapping during colorectal cancer surgeries: a systematic review and meta-analysis. *Dig Liver Dis*. 2020;52(12):1445–1454. doi:10.1016/j.dld.2020.08.020
17. Hameed S, Chen H, Irfan M, et al. Fluorescence guided sentinel lymph node mapping: from current molecular probes to future multimodal nanoprobes. *Bioconjug Chem*. 2019;30(1):13–28. doi:10.1021/acs.bioconjchem.8b00812
18. Alius C, Tudor C, Badiu CD, et al. Indocyanine green-enhanced colorectal surgery-between being superfluous and being a game-changer. *Diagnostics*. 2020;10(10):742. doi:10.3390/diagnostics10100742
19. Shi H, Yan R, Wu L, et al. Tumor-targeting CuS nanoparticles for multimodal imaging and guided photothermal therapy of lymph node metastasis. *Acta Biomater*. 2018;72:256–265. doi:10.1016/j.actbio.2018.03.035
20. Yang Z, Tian R, Wu J, et al. Impact of semiconducting perylene diimide nanoparticle size on lymph node mapping and cancer imaging. *ACS Nano*. 2017;11(4):4247–4255. doi:10.1021/acsnano.7b01261
21. Liu H, Yang Y, Liu Y, et al. Melanin-like nanomaterials for advanced biomedical applications: a versatile platform with extraordinary promise. *Adv Sci*. 2020;7(7):1903129. doi:10.1002/advs.201903129
22. Simon JD, Peles DN. The red and the black. *Acc Chem Res*. 2010;43(11):1452–1460. doi:10.1021/ar100079y
23. Lee H, Dellatore SM, Miller WM, Messersmith PB. Mussel-inspired surface chemistry for multifunctional coatings. *Science*. 2007;318(5849):426–430. doi:10.1126/science.1147241
24. Ge R, Lin M, Li X, et al. Cu^{2+}-loaded polydopamine nanoparticles for magnetic resonance imaging-guided ph- and near-infrared-light-stimulated thermochemotherapy [published correction appears in ACS Appl Mater Interfaces. 2021 Sep 22;13(37):45116-45117]. *ACS Appl Mater Interfaces*. 2017;9(23):19706–19716. doi:10.1021/acsami.7b05583
25. Hong L, Simon JD. Current understanding of the binding sites, capacity, affinity, and biological significance of metals in melanin. *J Phys Chem B*. 2007;111(28):7938–7947. doi:10.1021/jp071439h
26. Meng S, Kaxiras E. Mechanisms for ultrafast nonradiative relaxation in electronically excited eumelanin constituents. *Biophys J*. 2008;95(9):4396–4402. doi:10.1529/biophysj.108.135756
27. Ju KY, Lee Y, Lee S, Park SB, Lee JK. Bioinspired polymerization of dopamine to generate melanin-like nanoparticles having an excellent free-radical-scavenging property. *Biomacromolecules*. 2011;12(3):625–632. doi:10.1021/bm101281b
28. Huang C, Wang X, Yang P, et al. Size regulation of polydopamine nanoparticles by boronic acid and Lewis base. *Macromol Rapid Commun*. 2022:e2100916. PMID: 35080287. doi:10.1002/marc.202100916
29. Zou Y, Chen X, Yang P, et al. Regulating the absorption spectrum of polydopamine. *Sci Adv*. 2020;6(36):eabb4696. PMID: 32917617; PMCID: PMC7473670. doi:10.1126/sciadv.abb4696
30. Fu C, Zhou H, Wang Y, et al. One-pot synthesis of dextran-coated iron oxide nanoclusters for real-time regional lymph node mapping. *Int J Nanomedicine*. 2017;12:3365–3374. doi:10.2147/IJN.S130322
31. Jiang H, Wang Q, Sun X. Lymph node targeting strategies to improve vaccination efficacy. *J Control Release*. 2017;267:47–56. doi:10.1016/j.jconrel.2017.08.009
32. Liopo A, Su R, Oraevsky AA. Melanin nanoparticles as a novel contrast agent for optoacoustic tomography. *Photoacoustics*. 2015;3(1):35–43. doi:10.1016/j.pacs.2015.02.001
33. Fernandez-Fernandez A, Manchanda R, Lei T, et al. Comparative study of the optical and heat generation properties of IR820 and indocyanine green. *Mol Imaging*. 2012;11(2):99–113. doi:10.2310/7290.2011.00031
34. Bogusky MJ, Naylor AM, Pitzenberger SM, et al. NMR and molecular modeling characterization of RGD containing peptides. *Int J Pept Protein Res*. 1992;39(1):63–76. doi:10.1111/j.1399-3011.1992.tb01557.x
35. Liu D, Huang H, Zhao B, Guo W. Natural melanin-based nanoparticles with combined chemo/photothermal/photodynamic effect induce immunogenic cell death (ICD) on tumor. *Front Bioeng Biotechnol*. 2021;9:635858. doi:10.3389/fbioe.2021.635858
36. Samanen J, Ali F, Romoff T, et al. Development of a small RGD peptide fibrinogen receptor antagonist with potent antiaggregatory activity in vitro. *J Med Chem*. 1991;34(10):3114–3125. doi:10.1021/jm00114a022
37. Mas-Moruno C, Rechenmacher F, Kessler H. Cilengitide: the first anti-angiogenic small molecule drug candidate design, synthesis and clinical evaluation. *Anticancer Agents Med Chem*. 2010;10(10):753–768. doi:10.2174/187152010794728639

38. Huang Y, Li X, Sha H, et al. Tumor-penetrating peptide fused to a pro-apoptotic peptide facilitates effective gastric cancer therapy. *Oncol Rep*. 2017;37(4):2063–2070. doi:10.3892/or.2017.5440
39. Yang W, Noh J, Park H, et al. Near infrared dye-conjugated oxidative stress amplifying polymer micelles for dual imaging and synergistic anticancer phototherapy. *Biomaterials*. 2018;154:48–59. doi:10.1016/j.biomaterials.2017.10.043
40. Lan M, Zhao S, Liu W, Lee CS, Zhang W, Wang P. Photosensitizers for photodynamic therapy. *Adv Healthc Mater*. 2019;8(13):e1900132. doi:10.1002/adhm.201900132
41. Hou YJ, Yang XX, Liu RQ, et al. Pathological mechanism of photodynamic therapy and photothermal therapy based on nanoparticles. *Int J Nanomedicine*. 2020;15:6827–6838. doi:10.2147/IJN.S269321
42. Anzidei M, Napoli A, Zaccagna F, et al. Diagnostic performance of 64-MDCT and 1.5-T MRI with high-resolution sequences in the T staging of gastric cancer: a comparative analysis with histopathology. *Radiol Med*. 2009;114(7):1065–1079. doi:10.1007/s11547-009-0455-x
43. Sohn KM, Lee JM, Lee SY, Ahn BY, Park SM, Kim KM. Comparing MR imaging and CT in the staging of gastric carcinoma [published correction appears in AJR Am J Roentgenol 2000 Aug;175(2):556]. *AJR Am J Roentgenol*. 2000;174(6):1551–1557. doi:10.2214/ajr.174.6.1741551
44. Kim AY, Han JK, Seong CK, Kim TK, Choi BI. MRI in staging advanced gastric cancer: is it useful compared with spiral CT? *J Comput Assist Tomogr*. 2000;24(3):389–394. doi:10.1097/00004728-200005000-00006
45. Hasbahceci M, Akcakaya A, Memmi N, et al. Diffusion MRI on lymph node staging of gastric adenocarcinoma. *Quant Imaging Med Surg*. 2015;5(3):392–400. doi:10.3978/j.issn.2223-4292.2015.03.06
46. Giganti F, Orsenigo E, Arcidiacono PG, et al. Preoperative locoregional staging of gastric cancer: is there a place for magnetic resonance imaging? Prospective comparison with EUS and multidetector computed tomography. *Gastric Cancer*. 2016;19(1):216–225. doi:10.1007/s10120-015-0468-1
47. Loo BW Jr, Draney MT, Sivanandan R, et al. Indirect MR lymphangiography of the head and neck using conventional gadolinium contrast: a pilot study in humans. *Int J Radiat Oncol Biol Phys*. 2006;66(2):462–468. doi:10.1016/j.ijrobp.2006.05.045
48. Mitsumori LM, McDonald ES, Neligan PC, Maki JH. Peripheral magnetic resonance lymphangiography: techniques and applications. *Tech Vasc Interv Radiol*. 2016;19(4):262–272. doi:10.1053/j.tvir.2016.10.007
49. Manolova V, Flace A, Bauer M, Schwarz K, Saudan P, Bachmann MF. Nanoparticles target distinct dendritic cell populations according to their size. *Eur J Immunol*. 2008;38(5):1404–1413. doi:10.1002/eji.200737984
50. Ke X, Howard GP, Tang H, et al. Physical and chemical profiles of nanoparticles for lymphatic targeting. *Adv Drug Deliv Rev*. 2019;151–152:72–93. doi:10.1016/j.addr.2019.09.005
51. Zhang Y, Lin S, Wang XY, Zhu G. Nanovaccines for cancer immunotherapy. *Wiley Interdiscip Rev Nanomed Nanobiotechnol*. 2019;11(5):e1559. doi:10.1002/wnan.1559
52. Dong J, Ma Q. Integration of inflammation, fibrosis, and cancer induced by carbon nanotubes. *Nanotoxicology*. 2019;13(9):1244–1274. doi:10.1080/17435390.2019.1651920
53. Miyashiro I. What is the problem in clinical application of sentinel node concept to gastric cancer surgery? *J Gastric Cancer*. 2012;12(1):7–12. doi:10.5230/jgc.2012.12.1.7
54. Miyashiro I, Hiratsuka M, Sasako M, et al. High false-negative proportion of intraoperative histological examination as a serious problem for clinical application of sentinel node biopsy for early gastric cancer: final results of the Japan Clinical Oncology Group multicenter trial JCOG0302. *Gastric Cancer*. 2014;17(2):316–323. doi:10.1007/s10120-013-0285-3
55. Chen QY, Xie JW, Zhong Q, et al. Safety and efficacy of indocyanine green tracer-guided lymph node dissection during laparoscopic radical gastrectomy in patients with gastric cancer: a randomized clinical trial. *JAMA Surg*. 2020;155(4):300–311. doi:10.1001/jamasurg.2019.6033
56. Zhi D, Yang T, O'Hagan J, Zhang S, Donnelly RF. Photothermal therapy [published correction appears in J Control Release. 2020 Sep 16]. *J Control Release*. 2020;325:52–71. doi:10.1016/j.jconrel.2020.06.032
57. Doughty ACV, Hoover AR, Layton E, Murray CK, Howard EW, Chen WR. Nanomaterial applications in photothermal therapy for cancer. *Materials*. 2019;12(5):779. doi:10.3390/ma12050779
58. Jayapaul J, Arns S, Bunker M, et al. *In vivo* evaluation of riboflavin receptor targeted fluorescent USPIO in mice with prostate cancer xenografts. *Nano Res*. 2016;9(5):1319–1333. doi:10.1007/s12274-016-1028-7